Inorganic Chemistry

ARTICLE

pubs.acs.org/IC

Smart Heterostructures for Tailoring the Optical Properties of Photochromic Hybrid Organic−Inorganic Polyoxometalates

Rémi Dessapt,* Marie Gabard, Martine Bujoli-Doeuff, Philippe Deniard, and Stéphane Jobic

Institut des Matériaux Jean Rouxel, Université de Nantes, CNRS, 2 rue de la Houssinière, BP 32229, 44322 Nantes, France

S *Supporting Information*

ABSTRACT: A new concept of photoresponsive composites has been elaborated by intimately connecting a Photochromic Phase (PP), $(H_2DABCO)_2(HDMA)_{0.5}Na_{0.75}(H_3O)_{0.75}[Mo_8O_{27}]\cdot 3H_2O$ (**1**), with a second hybrid organic−inorganic molybdate material, $(H_2DABCO)(HDABCO)[Fe(OH)_6Mo_6O_{18}]\cdot 4H_2O$ (**2**) acting as an Oxidation Catalytic Phase (OCP) toward the former once photoexcited. The association of both the PP and the OCP in the composite drastically improves the bleaching process of the PP alone because of efficient electronic transfers through the OCP-PP interface without affecting significantly its photoinduced color change characteristic. Two OCP-PP composites with different PP weight percents have been obtained by associating **1** with **2**. The optical properties of these composites before and after UV irradiation have been investigated by Diffuse Reflectance Spectroscopy, and the strong impact of the OCP on the fading kinetics of the PP has been clearly highlighted.

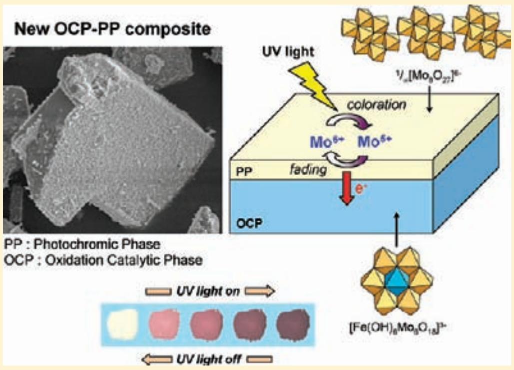

1. INTRODUCTION

Photochromism refers to the ability of some substances, organic,[1] inorganic,[2] and hybrid organic−inorganic[3] to undergo a reversible color change in response to light exposure. Such materials are of interest for potential applications as smart windows, cosmetics, multicolor smart painting, UV sensors, optical power-limiting switches, and three-dimensional (3D) high-density optical data storage. In these fields, challenging developments necessitate the elaboration of new photoresponsive devices that can be miniaturized at will. With this aim, materials built upon polyoxomolybdates (Mo-POMs) following a bottom-up approach constitute an attractive answer. Mo-POMs[4] are anionic metal oxide building blocks which can be assembled with organoammonium cations (OACs) in a wide range of hybrid organic−inorganic networks.[5] Mo-POM/OAC materials show remarkable surface-limited photochromic responses[6] in air, Ar atmosphere, and under vacuum, including very high coloration contrasts and fast coloration speed, compared to pure inorganic photochromic devices. Additionally, they offer a wide photogenerated color range. Their photochromic performances (notably in terms of coloration speed and contrast) compete with that of purely organic photoactive molecules in the solid state, and they are better temperature and UV resistant. In addition, they present several advantages for the design of new photochromic devices, such as low density, transparency, and processability. The photochromic properties of such materials originate from a synergetic mechanism taking place at the organic−inorganic interface.[6a] Namely, the physical process involved implies the photoreduction of Mo^{6+} cations into Mo^{5+} ones within the Mo-POM block, with a concomitant displacement of a labile hydrogen atom from the $N^+{-}H$ bond of the organic component to the mineral one. The chemical levers at our disposal to tune their photoresponses have been identified.[6c] To sum up, the photogenerated hue depends on both the chemical composition and the topology of the Mo-POMs, whatever the nature of the associated OACs. The wide palette of photoinduced coloration originates from the great diversity of sizes, nuclearities, and shapes of the Mo-POM units. In addition, our recent works highlighted that the coloration speed can be controlled by choosing the appropriate OACs.[7] Explicitly, within a series of hybrid materials containing the same Mo-POM block and an identical hydrogen bond network at the organic−inorganic interface, the lower the homolytic dissociation energy of the $N^+{-}H$ bond, the faster the color change. Their use as fast reversible photoresponsive devices in air is unfortunately limited so far by their slow bleaching speeds once UV excitation is turned off (for indication, no bleaching reaction occurs under Ar atmosphere or under vacuum). Formally, the fading mechanism, which implies the back oxidation of the photoreduced Mo^{5+} centers by O_2[6b], is not fully understood. Nevertheless, the efficiency of the oxidation mechanism is probably limited because of the poor interaction between the Mo^{5+} cations in the solid phase and the gaseous oxidizing agent.

We report in this paper a new strategy to speed up the fading kinetics of Mo-POM/OAC Photochromic phases (PP). It consists in elaborating composites obtained by connecting intimately a PP with a material acting as an Oxidation Catalytic phase

Received: March 30, 2011
Published: August 22, 2011

(OCP) within a heterostructure. The OCP should contain an oxidizing agent (for example a POM unit with a reducible heterometallic cation as Fe^{3+}) being located in the vicinity of the photogenerated Mo^{5+} cations of the PP, to improve, after cutting off the UV light excitation, their back-oxidation via efficient electronic transfers from the PP to the OCP through the interface. Three additional criteria can be enacted to direct the choice of such an appropriate OCP. They are listed below:

(1) The OCP should be colorless to avoid any modifications of the chromatic characteristics of the PP in its ground state. On this basis, the OCP should be a semiconductor with an optical band gap greater than 3 eV, and a refractive index similar to that of the PP to limit diffusion effects.

(2) The OCP should not absorb the UV energy needed to activate the photochromic process of the PP. So, the OCP should have an optical band gap (much) higher than the PP.

(3) The OCP should not modify the photogenerated hue of the PP after UV excitation. So, the OCP should not possess any photochromic properties.

In this work, $(H_2DABCO)_2(HDMA)_{0.5}Na_{0.75}(H_3O)_{0.75}[Mo_8O_{27}]\cdot 3H_2O$ (**1**)[8,9] has been chosen as the PP. This material is one of the most efficient photochromic Mo-POM materials in terms of coloration contrast and coloration speed.[7] We have postulated that the association of both a PP and an OCP which contain a common OAC should be pertinent to design a well organized interface between both materials in the composite. Hence, we have synthesized a new hybrid organic−inorganic material, namely, $(H_2DABCO)(HDABCO)[Fe(OH)_6Mo_6O_{18}]\cdot 4H_2O$ (**2**). This material contains the Anderson−Evans $[Fe(OH)_6Mo_6O_{18}]^{3-}$ anion[10] (hereafter labeled $FeMo_6$) and has all the required criteria to be used as efficient OCPs (see below). In section 2, we report the synthesis of **2**, and we describe the experimental procedures to prepare two new OCP-PP composites containing 50% and 15% in weight of PP, by coupling **1** and **2**. The structural and morphological characterization of **2**, and the composites are reported in section 3.1.

The optical properties of the materials before UV irradiation have been described in section 3.2. We have quantitatively investigated the coloration and fading kinetics of the composites such as the pure **1** from the evolution in time of their diffuse reflectivity spectra in ambient conditions. A fading kinetics model has been proposed which describes the time dependence of the oxidation of the Mo^{5+} cations into Mo^{6+} ones during the fading process. The efficiency of the OCP to drastically speed up the bleaching process of the PP in the composite has been highlighted. The essential finding of our work is summarized in section 4.

2. EXPERIMENTAL SECTION

Synthesis. 1,4-Diazabicyclo[2.2.2]octane $N_2C_6H_{12}$ (DABCO), dimethylamine hydrochloride NC_2H_8Cl (DMA.HCl), $Na_2MoO_4\cdot 2H_2O$, and $FeCl_3\cdot 6H_2O$ were purchased from Aldrich. All reagents were used without further purification.

$(H_2DABCO)_2(HDMA)_{0.5}Na_{0.75}(H_3O)_{0.75}[Mo_8O_{27}]\cdot 3H_2O$ (1). **1** has been synthesized according to the reported procedure.[7]

$(H_2DABCO)(HDABCO)[Fe(OH)_6Mo_6O_{18}]\cdot 4H_2O$ (2). $Na_2MoO_4\cdot 2H_2O$ (6.776 g, 28 mmol) was dissolved in water (60 mL), and the solution was put in an ice bath. The pH was then adjusted to 6 with 5 M HCl. After addition of $FeCl_3\cdot 6H_2O$ (1.260 g, 4.66 mmol), the pH was adjusted again until it reached 4. The so-obtained colorless solution (solution 1) was stirred for 2 h at low temperature, and kept at room temperature. In addition, a second solution (solution 2) is obtained by dissolving DABCO (1.260 g, 11.25 mmol) in water (20 mL) at room temperature, and the pH was adjusted with 5 M HCl until it reached 4. Solution 2 was mixed to solution 1 under vigorous stirring leading to the fast precipitation of a white solid of **2**. The mixture was stirred at room temperature for 1 h, and then filtered. The powder was washed with H_2O, and EtOH, and dried in air (yield in Mo: 97%). *Anal.* Calcd for $C_{12}H_{41}O_{28}N_4FeMo_6$: C, 10.91; H, 3.13; N, 4.24; Fe, 4.23; Mo, 43.58. Found: C, 11.03; H, 3.14; N, 4.14; Fe, 4.20; Mo, 43.50. FT-IR (cm^{-1}): H_2O, 1643 (w), 1614 (w); H_2DABCO^{2+}, $HDABCO^{+}$ cations, 1470 (w), 1462 (m), 1396 (w), 1325 (w), 1313 (w), 1196 (sh), 1169 (sh), 1051 (m), 1030 (sh); ν(Mo−O), ν(Fe−O), 935 (s), 928 (s), 889 (s), 878 (vs), 843 (s), 806 (m), 783 (m), 731 (w), 602 (vs), 555 (vs), 503 (s), 430 (w). From DSC/TGA measurements, **2** is stable up to 140 °C.

Crystals of **2** suitable for X-ray structure analysis have been obtained as followed. $Na_2MoO_4\cdot 2H_2O$ (6.776 g, 28 mmol) was dissolved in water (60 mL). After addition of DABCO (1.260 g, 11.2 mmol), the pH was adjusted to 6 with 5 M HCl. $FeCl_3\cdot 6H_2O$ (1.260 g, 4.66 mmol) was added, and the pH was adjusted with 5 M HCl until it reached 4. The mixture was stirred at room temperature for few minutes, and the mixture was sealed in a 30 mL Teflon-lined autoclave (130 °C, 2 days, autogenous pressure). The slurry was filtered to remove a brown precipitate, and the solution was left at ambient temperature. Colorless crystals of **2** were isolated from the solution after a few days.

OCP-PP50. $Na_2MoO_4\cdot 2H_2O$ (1.000 g, 4.13 mmol) was dissolved in water (60 mL). After addition of DABCO (0.140 g, 1.25 mmol) and DMA.HCl (0.450 g, 5.52 mmol), the pH was slowly adjusted to 6 with 5 M HCl. After addition of pure powder of **2** (0.800 g, 6.06 mmol), the pH was adjusted with 5 M HCl, until it reached 4. The mixture was stirred at room temperature for 3 h, and was then filtered to isolate a pale yellow solid. The powder was washed with H_2O, EtOH, and dried in air. *Anal.* Calcd: Fe, 2.11. Found: Fe, 2.15.

A similar procedure has been used to obtain **OCP-PP15**, using $Na_2MoO_4\cdot 2H_2O$ (0.252 g, 1.04 mmol), DABCO (0.039 g, 0.35 mmol), DMA·HCl (0.246 g, 3.02 mmol), and **2** (0.800 g, 6.06 mmol). *Anal.* Calcd: Fe, 3.17. Found: Fe, 3.19. Used powders of **2** in both OCP-PP50 and OCP-PP15 were issued from the same synthesis batch.

Structure Determination. Crystals of **2** were glued at the tip of Lindemann capillaries by means of solvent free glue. Diffraction intensities were collected at 293 K on a Bruker-Nonius KappaCCD diffractometer equipped with graphite-monochromated MoK-$L_{2,3}$ radiation (0.71073 Å), by using the φ- and ω-scan technique. The structures were initially solved by the Sir2004 direct methods,[11] completed, and refined with the full-matrix least-squares technique using the Jana2006 program,[12] and drawn with the Diamond program.[13] Residual factors are given in Table 1. CCDC 803803 contains the supplementary crystallographic data for this paper. These data can be obtained free of charge via www.ccdc.cam.ac.uk/conts/retrieving.html (or from the Cambridge Crystallographic Data Centre, 12 Union Road, Cambridge CB21EZ, U.K.; fax: (44) 1223−336−033; e-mail: deposit@ccdc.cam.ac.uk). The powder purity of **2** has been checked, from the comparison of its patterns with its structure as determined from single crystals (Supporting Information, Figure S1).

Physical Measurements. Powder X-ray patterns were collected at room temperature on a Bruker D8 advance diffractometer equipped with graphite-monochromated CuK-L3 (1.540598 Å); Bragg−Brentano geometry; linear detector; 2θ range = 8−60°). SEM images were taken in a high magnification microscope JEOL JSM-6400F. For SEM studies, sample preparations were done by spreading a little amount of powder on a carbon tape pasted over a copper metal sample holder. Direct current (dc) magnetic measurements were performed on a Quantum Design MPMS-5S SQUID magnetometer at temperatures ranging from 2 to 300 K. Supporting Information, Figure S3, shows plots of the inverse

Table 1. Crystallographic Data of **2**

	2
(a) Physical, Crystallographic, and Analytical Data	
empirical formula	$FeMo_6O_{28}N_4C_{12}H_{41}$
M_r (g mol^{-1})	1320.9
cryst syst, space group	triclinic, $P\bar{1}$
a (Å)	8.1557(4)
b (Å)	9.4304(12)
c (Å)	11.6154(12)
α (deg)	76.731(9)
β (deg)	83.603(7)
γ (deg)	84.950(7)
V (Å^3)	862.30(11)
Z	1
F_{000}	642
D_x (g cm^{-3})	2.541
radiation λ (Å)	Mo K-$L_{2,3}$ 0.71069
μ (mm^{-1})	2.62
T (K)	293
cryst shape, size	plate, white
cryst dimens (mm)	0.28 × 0.05 × 0.02
(b) Data Collection and Data Reduction	
diffractometer	Nonius CCD
radiation source	Mo K-$L_{2,3}$
monochromator	graphite
scan mode	φ, ω scans
absorption correction	Gaussian Jana2006 (Petricek, Dusek, and Palatinus, 2000)
transmission	$T_{min} = 0.667$, $T_{max} = 0.950$
measured reflections	32192
independent reflections	7418
reflections with $I > 2\sigma(I)$	5034
R_{int}	0.053
θ_{max}	35°
θ_{min}	6.4°
	$h = -13 \rightarrow 12$
	$k = -15 \rightarrow 15$
	$l = -18 \rightarrow 18$
(c) Refinement	
refinement	F^2
$R[F^2 > 2\sigma(F^2)]$	0.033
$wR(F^2)$	0.078
S	1.28
nbr. reflections	7418
nbr. parameters	265
nbr. constraints	48
weighting scheme	$w = 1/(\sigma^2(I) + 0.001936I^2)$
$\Delta\rho_{max}$	1.02 e Å^{-3}
$\Delta\rho_{min}$	−1.86 e Å^{-3}
extinction correction	B−C type 1 Lorentzian isotropic (Becker and Coppens, 1974)

molar susceptibilities obtained at $H = 5$ kOe in the range 2−300 K on the powder of **2**. Susceptibility data were fitted to a Curie−Weiss law, $\chi = C/(T - \theta)$. The fitted values of the Curie constant (C, expressed in cm^3 K mol^{-1}), the Weiss temperature (θ), and the paramagnetic moment, $\mu = (8C)^{1/2}$ (expressed in μ_B) are given in the figure. Elemental analyses of the solids were performed by the "Service d'Analyse du CNRS", in Vernaison (France). FT-IR spectra were recorded in the 4000−400 cm^{-1} range on a BRUKER Vertex equipped with a computer control using the OPUS software. Differential scanning calorimetry (DSC) and thermogravimetric analysis (TGA) were performed by flowing dry argon with a heating and cooling rate of 5 °C/min on a SETARAM Tg-DSC 111 between 20 and 800 °C. Diffuse reflectivity spectra were collected at room temperature on a finely ground sample with a Cary 5G spectrometer (Varian) equipped with a 60 mm diameter integrating sphere and computer control using the "Scan" software. Diffuse reflectivity was measured from 250 to 1550 nm (i.e., from 5 to 0.8 eV) with a 2 nm step using Halon powder (from Varian) as reference (100% reflectance). The reflectivity data were treated by a Kubelka−Munk transformation[14] to obtain the corresponding absorption data and hence better locate the absorption thresholds. The samples were irradiated with a Fisher Bioblock labosi UV lamp (λ_{exc} = 365 or 254 nm, P = 12 W).

3. RESULTS AND DISCUSSION

3.1. Synthesis. A new hybrid material has been synthesized, namely, $(H_2DABCO)(HDABCO)[Fe(OH)_6Mo_6O_{18}]\cdot 4H_2O$ **2**. **2** has been obtained as a white powder at room temperature under atmospheric pressure, and single crystals have been isolated under hydrothermal conditions at 130 °C, after filtration and slow evaporation of the medium. The single-crystal X-ray analysis of **2** (Table 1) has confirmed that it contains the $FeMo_6$ anion (Figure 1a). This unit is built upon six edge-shared distorted $[MoO_5(OH)]$ octahedra defining a closed $[Mo_6O_{18}(OH)_6]$ ring which encapsulates a Fe^{3+} cation. The $FeMo_6$ clusters and the water molecules are connected via a complex hydrogen bonding subnetwork, to form $^2/_\infty\{(H_2O)_4[Fe(OH)_6Mo_6O_{18}]\}^{3-}$ layers parallel to the *ab* plane (Figure 1b). Mono- and diprotonated DABCO cations are linked together via a common hydrogen atom to form linear $[H_3(DABCO)_2]^{3+}$ cations (Figure 1c). These latter connect two $FeMo_6$ entities of two adjacent $^2/_\infty\{(H_2O)_4[Fe(OH)_6Mo_6O_{18}]\}^{3-}$ layers via strong hydrogen bonding interactions ($d_{N\cdots O}$ = 2.655(4) Å) (Figure 1d) to form a supramolecular 3D network.

The presence of the $FeMo_6$ unit in **2** has been also clearly evidenced by elemental analysis, FT-IR spectroscopy (Supporting Information, Figure S2) and magnetic measurements (Supporting Information, Figure S3). As expected, the observed magnetic moment in **2** is consistent with the presence of Fe^{3+} ions with a high spin configuration ($S = 5/2$).

Two OCP-PP composites containing 50% and 15% in weight of **1** (hereafter noticed as OCP-PP50 and OCP-PP15, respectively) have been realized. Our strategy has consisted in inducing the precipitation of **1** at the surface of **2** crystals. Practically, a microcrystallized **2** powder has been dispersed in an aqueous solution containing MoO_4^{2-}, DABCO, and $HDMA^+$ molecules, that is, the precursors of **1**. The quantitative precipitation of **1** has been then pH-monitored. Both OCP-PP50 and OCP-PP15 composites have been characterized by powder XRD analyses (Supporting Information, Figure S4). Patterns are the perfect superimposition of those of **1** and **2**. The diffraction peaks of **2** are sharp, indicating the highly crystalline character of this material, while those of **1** are broad, revealing small crystallite size. SEM observations show the same trend: both composites contain large well shaped **2** crystals (with a mean size of few

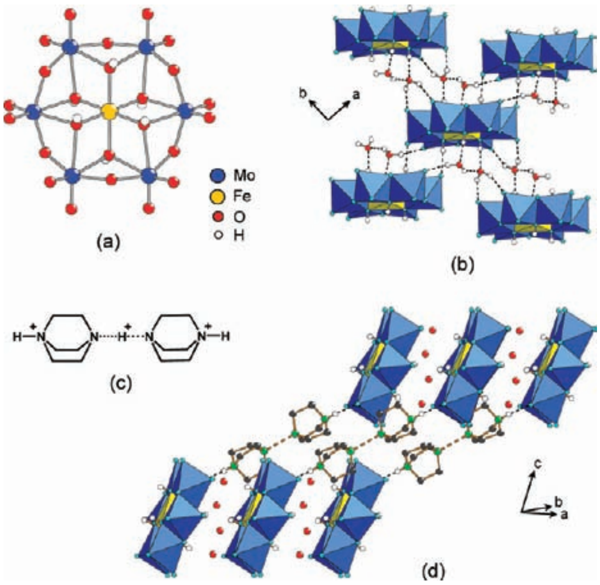

Figure 1. (a) Ball and stick representation of the $[Fe(OH)_6Mo_6O_{18}]^{3-}$ anion ($FeMo_6$) in **2**. (b) Representation of the complex hydrogen bonding networks between the $FeMo_6$ entities and the water molecules to form the $^2/_\infty\{(H_2O)_4[Fe(OH)_6Mo_6O_{18}]\}^{3-}$ layer in the *ab* plane. (c) Schematic representation of the $[H_3(DABCO)_2]^{3+}$ cation in **2**. (d) Representation of the organic−inorganic connection in **2**. The connection between the $^2/_\infty\{(H_2O)_4[Fe(OH)_6Mo_6O_{18}]\}^{3-}$ layers is ensured via the $[H_3(DABCO)_2]^{3+}$ cations with short hydrogen bonding interactions (dotted lines). For clarity, the hydrogen atoms of the CH_2 groups in DABCO molecules are omitted.

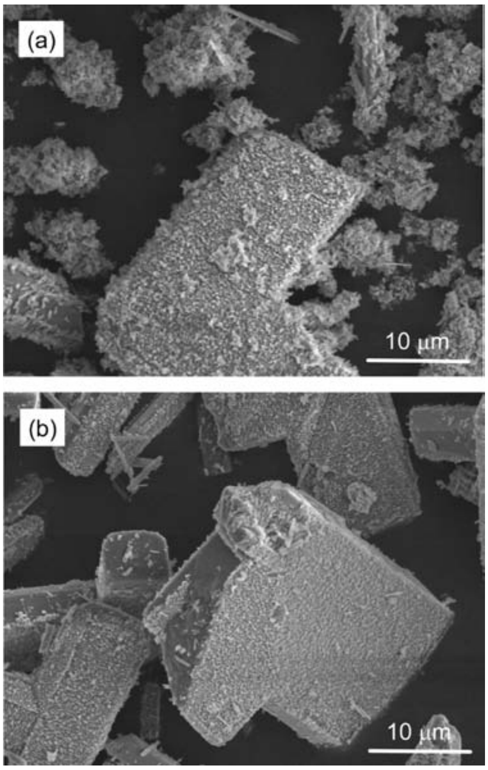

Figure 2. (a) SEM images of the OCP-PP50 composite (50% in weight of **1**) showing the mixture of pure phase of **1** and **1@2**. (b) SEM image of a selected **1@2** heterostructure in the OCP-PP15 composite (15% in weight of **1**).

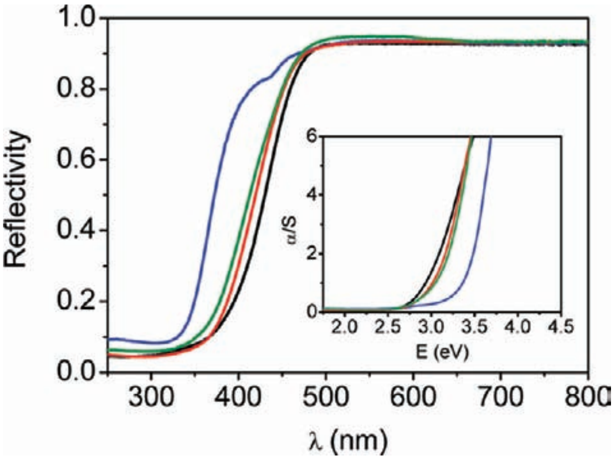

Figure 3. Diffuse reflectivity vs wavelength of **1** (black solid line), **2** (blue solid line), OCP-PP15 (green solid line), and OCP-PP50 (red solid line) in the 250−800 nm range. Inset: Kubelka−Munk transformed reflectivity vs energy of **1** (black solid line), **2** (blue solid line), OCP-PP15 (green solid line), and OCP-PP50 (red solid line).

micrometers), and smaller **1** crystals (with a mean size around 100 nm). Figure 2a shows that the OCP-PP50 sample is a mixture of **2** microcrystals largely covered by **1** nanocrystals (**1@2**) and bundles of pure **1** phase. This suggests that the PP/OCP weight ratio is too high to deposit the whole amount of **1** only on the surface of **2**. In contrast, the SEM image of OCP-PP15 (Figure 2b) shows only **2** microcrystals partially covered by **1** nanocrystals (**1@2**) without any isolated bundles of pure **1** phase. We notice that **1** seems to be preferentially deposited on specific crystal faces of **2**. At first sight, this oriented coating of **1** over **2** hints a directed growth of **1** on privileged faces of **2**, with the formation of organized interfaces. This may be related to the presence of DABCO molecules in both **1** and **2** which could serve of pseudoseed to an interface growth mechanism. So far, this hypothesis cannot be proved by HRTEM because of the strong sensitivity of the hybrid materials toward electron beams.

3.2. Optical Characterizations. **2** fulfills the three criteria defined above for the OCP. This material is colorless with an optical band gap of 3.42 eV, that is, a value much higher than that of **1** (2.95 eV). In addition, **2** turns out to be photochromic neither under 365 nm (3.40 eV) nor 254 nm (4.88 eV) UV irradiation, even after excitation for periods as long as half a day. At first sight, we suspect that this lack of photoresponses (in spite of the presence of strong hydrogen bonding interactions between the $FeMo_6$ anions and the OACs in **2**) is related to the too short lifetime of the photogenerated Mo^{5+} cations because of the proximity of the central Fe^{3+} cation and its strong propensity to capture the photogenerated electron on the molybdenum site.

The diffuse reflectivity spectra of **1**, **2**, OCP-PP50, and OCP-PP15 are given in Figure 3. **1**, OCP-PP50 and OCP-PP15 show a similar yellow pale coloration in their ground state. This is evidence that the presence of **2** in the composites does not noticeably impact the overall optical characteristics of **1** in the 250−800 nm range. OCP-PP50 and OCP-PP15 display an absorption threshold at 3.05 and 3.22 eV, respectively, that is, intermediate values between those of pure **1** and **2**.

Under 365 nm (3.4 eV) UV irradiation in ambient conditions, the color of **1**, OCP-PP50, and OCP-PP15 shifts from yellow

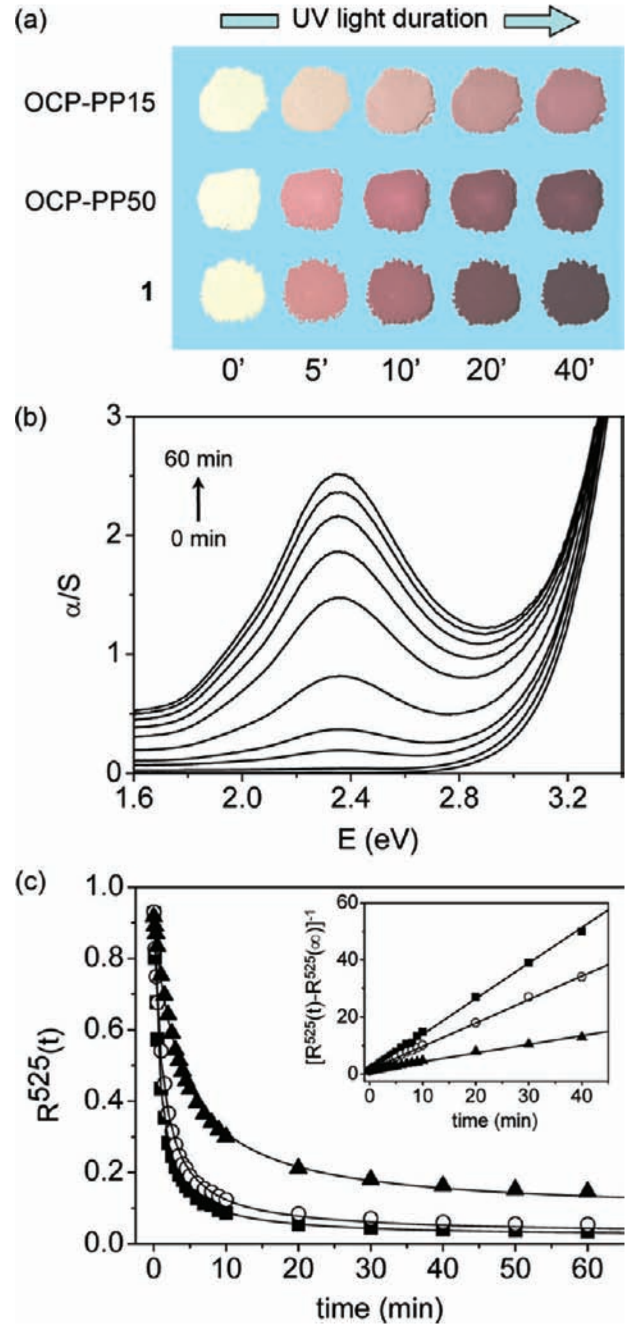

Figure 4. (a) Color of **1**, OCP-PP50, and OCP-PP15 at different 365 nm UV-light irradiation times. (b) Kubelka–Munk transformed reflectivity of OCP-PP15 after 0, 1, 3, 5, 10, 20, 30, 40, 50, and 60 min of UV irradiation at 365 nm. (c) Reflectivity $R^{525}(t)$ versus t plots for (▲) OCP-PP15, (○) OCP-PP50, and (■) **1**. The inset shows linear $[R^{525}(t) - R^{525}(\infty)]^{-1}$ versus t plots for the three samples.

Table 2. Salient Parameters Related to the Coloration and Fading Kinetics Change of 1, OCP-PP50 and OCP-PP15

	1	OCP-PP50	OCP-PP15
	Coloration		
k_{ci}/k_{c1}	1.00	0.72	0.26
R^{2a}	0.9987	0.9986	0.9983
	Fading		
k_f (min^{-1})	2.00×10^{-4}	1.29×10^{-3}	2.50×10^{-3}
k_{fi}/k_{f1}	1.00	6.15	12.50
R^{2b}	0.9960	0.9996	0.9970

[a] Regression coefficients for the $R^{525}(t)$ vs t plots. [b] Regression coefficients for the $\ln[(R^{525}(t) - R^{525}(0))/(0.3 - R^{525}(0))]$ vs t plots.

pale to faint purple, the tint becoming darker and darker when irradiation time is increased, to finally reach a eye-detected saturation level after 40 min (Figure 4a). At any irradiation time t, the hue intensity follows the sequence **1** > OCP-PP50 > OCP-PP15, in agreement with the dilution of the PP in the composites. The irradiation time dependence of absorption of OCP-PP15 is displayed in Figure 4b. As expected on the basis of a previous investigation of **1**,[7] the color change in the composite is associated with a broad absorption band peaking at 525 nm (2.36 eV), which intensity gradually increases with irradiation time. The coloration kinetics of OCP-PP50 and OCP-PP15 have been quantified by analyzing the evolution of the diffuse reflectivity values at 525 nm as a function of the irradiation time t. The $R^{525}(t)$ versus t curves are displayed in Figure 4c and compared with that of **1**. On the basis of the model we recently developed,[7] the decrease of the $R^{525}(t)$ values with the irradiation time is correlated to the decrease of the concentration of reducible Mo^{6+} cations in the PP, which occurs according to a pseudo second-order kinetic law (see Supporting Information for the details of the coloration kinetic model). Hence, the $R^{525}(t)$ versus t curves can be perfectly fitted by the eq 1.

$$R^{525}(t) = a/(bt + 1) + R^{525}(\infty) \qquad (1)$$

$R^{525}(\infty)$ is the reflectivity value at the end of the photochromic process, that is, at $t = \infty$. The a parameter is defined as $a = R^{525}(0) - R^{525}(\infty)$, that is, the difference between the reflectivity values just before UV illumination ($t = 0$), and at $t = \infty$. The b parameter is defined as $b = k_c \times C_{6+,r}(0)$, where k_c is the coloration rate constant, and $C_{6+,r}(0)$ is the initial concentration of photoreducible Mo^{6+} centers in the materials.

Three main observations can be deduced from the $R^{525}(t)$ versus t curves. First, the three materials have quite similar high $R^{525}(0)$ values. This agrees well with the fact that none of the samples absorbs at 525 nm before UV irradiation. Second, $R^{525}(\infty)$ turns out to be lower for **1** than for the OCP-PP phases, and it increases when decreasing the quantity of the PP in the composites. This is the expected trend since $R^{525}(\infty)$ is directly correlated to $C_{6+,r}(0)$ (Supporting Information), that is, the $R^{525}(\infty)$ value increases with the dilution of the reducible Mo^{6+} cations in the composite. However, the presence of bundles of pure phase of **1** in quite large amount in OCP-PP50 could explain why this sample shows a $R^{525}(t)$ versus t curve similar to that of **1**. Let us mention that the calculated degree of photoreduction (Supporting Information) after 60 min of UV irradiation is 93%, 97%, and 98% for OCP-PP15, OCP-PP50, and **1**, respectively. This shows that the photochromic process of the three samples is quasi complete after 1 h. Third, although OCP-PP50 and OCP-PP15 show strong eye-detectable photochromic effects, the presence of **2** has a noticeable influence on the coloration speed of the composites. Table 2 sums up the kinetic parameters related to the color change of **1**, OCP-PP50, and OCP-PP15, respectively. The relative coloration rate constants k_{ci}/k_{c1} ratios (Supporting Information), which can be extracted from the slopes of the linear $[R^{525}(t) - R^{525}(\infty)]^{-1}$ versus

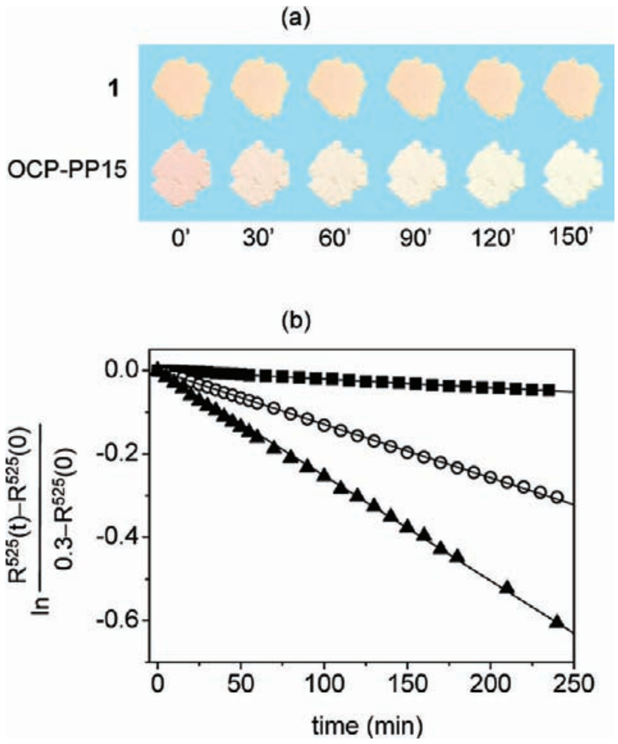

Figure 5. (a) Evolution of the color of **1** and OCP-PP15 once irradiated for 1.9 and 10.8 min respectively, 0, 30, 60, 90, 120, and 150 min after cutting off the UV excitation (the starting color of OCP-PP15 and **1** is a little bit different because of a yellowish-white coloration before UV excitation more pronounced for **1** than for OCP-PP15). (b) $\ln[(R^{525}(t) - R^{525}(0))/(0.3 - R^{525}(0))]$ vs t plots for (▲) OCP-PP15, (○) OCP-PP50, and (■) **1**.

Scheme 1. Representation of the Possible Fast Indirect Oxidation Mechanism at the OCP-PP Interface

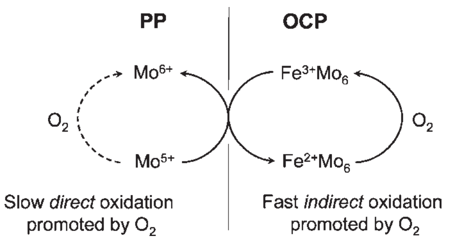

t plots (see inset of Figure 4c), decreases from 1 to 0.72, and 0.26 going from **1** to OCP-PP50, and OCP-PP15. These trends can be interpreted considering the observed color change of the composites as the sum of two opposite processes. Hence, on one side, the UV light excitation leads to the reduction of Mo^{6+} cations into Mo^{5+} ones in **1** and, on the other side, the back oxidation of Mo^{5+} cations is strongly catalyzed by **2** at the interface with **1**, so that the color change of the composites is slowed down compared to **1** alone. Hence, k_{ci} should be viewed as apparent coloration rate constants. These results evidence the efficiency of **2** to act in air as a better oxidizing agent than O_2 alone for UV-light-exposed PP.

The fading kinetics of **1**, OCP-PP50, and OCP-PP15 have been investigated in ambient conditions. The three samples were irradiated under a 365 nm UV light for 1.9, 2.8, and 10.8 min, respectively, until $R^{525}(t)$ arbitrarily reached the 0.3 value, that is, the three samples contains the same quantity of photogenerated Mo^{5+} cations per volume unit of **1**, which corresponds to the reduction of about 70% of photoreducible Mo^{6+} cations (Supporting Information). Then, after turning off the UV excitation, the purple color of OCP-PP15 gradually fades in intensity and totally disappears after the sample is kept for about 2 h in ambient conditions (Figure 5a). As expected, the fading process is faster for OCP-PP15 than for pure **1**. The fading kinetics of the materials were quantified by analyzing the evolution of $R^{525}(t)$ as a function of time. Details of the fading kinetics model are given in Supporting Information. The decrease in the Mo^{5+} concentration with the time occurs according to a pseudo first-order kinetic law, and not a second-order kinetic one as observed for the coloration process. These results clearly confirm two different mechanisms for both the coloration and bleaching processes. The fading rate constants (k_f) of the materials can be extracted from the slope of the linear $\ln[(R^{525}(t) - R^{525}(0))/(0.3 - R^{525}(0))]$ versus t plots (Figure 5b), according to eq 2.

$$\ln[(R^{525}(t) - R^{525}(0))/(0.3 - R^{525}(0))] = -k_f \times t \qquad (2)$$

k_f increases in the sequence **1** < OCP-PP50 < OCP-PP15 (Table 2) as clearly evidenced in Figure 5. For OCP-PP15, k_f is enhanced by a factor ~12 compared to **1** alone, which proves that, in ambient conditions, the $FeMo_6$ anions in **2** strongly catalyze the back oxidation of the photogenerated Mo^{5+} cations in **1**. However, the purple color of OCP-PP15 is maintained for a long period when the composite is kept in a O_2-free atmosphere. This implies that, similarly as it is observed for pure **1**, the oxidation of the Mo^{5+} cations in the **1**@**2** heterostructure needs the presence of O_2. Consequently, the fading process in OCP-PP15 should occur according to the fast indirect oxidation mechanism depicted in Scheme 1. In a first step, the $Fe^{III}Mo_6$ anions in **2** oxidize the photogenerated Mo^{5+} cations in **1** via efficient electronic transfers from **1** to **2** through the interface of the composite. In a second step, the unstable reduced $Fe^{II}Mo_6$ units are quickly oxidized by O_2 to regenerate $Fe^{III}Mo_6$ entities.

4. CONCLUSION

We have developed a new class of photoresponsive composites which associates a photochromic molybdate (PP) and an oxidizing catalytic phase (OCP) containing the Fe-Anderson ($FeMo_6$) anion as the oxidizing agent. The oriented growth of the PP on the OCP induces a well organized interface which favors efficient electronic transfers (which remain to be optimized) from the PP to the OCP after switching off the UV excitation. The fading kinetics of the composites have been quantitatively investigated in ambient conditions, and we have demonstrated that the $FeMo_6$ anions strongly catalyze the back oxidation of the photoreduced Mo^{5+} cations in the PP, better than O_2 alone. Despite the coloration kinetics of the as-described composites remain still faster than the fading ones, our concept of OCP-PP composites opens up a new way to the elaboration of efficient and tunable reversible photochromic hybrid organic–inorganic polyoxometalate materials. To date, a dozen coloration/fading cycles have been performed on OCP-PP15 without detecting any fatigue resistance. The optimization of the bleaching performances of the composites is now under study. In particular, we are thus working on a better characterization of the OCP/PP interface to elucidate the role played by the common protonated DABCO molecules in the oriented growth of the PP on the OCP. In addition, the electronic transfer process from the PP to the OCP through the interface is not yet well understood, and its understanding will be deepened in future work.

■ ASSOCIATED CONTENT

Ⓢ Supporting Information. Single crystals X-ray diffraction data of **2**, FT-IR spectroscopy and magnetic measurements of **2**, powder XRD analyses of **1**, **2**, and the composites). Complementary detailed coloration and fading kinetics models. This material is available free of charge via the Internet at http://pubs.acs.org.

■ AUTHOR INFORMATION

Corresponding Author

*E-mail: remi.dessapt@cnrs-imn.fr. Phone: +33 2 40 37 39 53. Fax: +33 2 40 37 39 95.

■ ACKNOWLEDGMENT

The authors are grateful to Pr Christophe Payen, Institut des Matériaux Jean Rouxel, France, for the magnetic measurements.

■ REFERENCES

(1) (a) Berkovic, G.; Krongauz, V.; Weiss, V. *Chem. Rev.* **2000**, *100*, 1741–1753. (b) Irie, M. *Chem. Rev.* **2000**, *100*, 1685–1716. (c) Kawata, S.; Kawata, Y. *Chem. Rev.* **2000**, *100*, 1777–1788. (d) Corredor, C. C.; Huang, Z.-L.; Belfield, K. D.; Morales, A. R.; Bondar, M. V. *Chem. Mater.* **2007**, *19*, 5165–5173. (e) Wen, Y.; Wang, J.; Hu, J.; Jiang, L.; Gao, H.; Song, Y.; Zhu, D. *Adv. Mater.* **2006**, *18*, 1983–1987. (f) Miyasaka, H.; Satoh, Y.; Ishibashi, Y.; Ito, S.; Nagasawa, Y.; Taniguchi, S.; Chosrowjan, H.; Mataga, N.; Kato, D.; Kikuchi, A.; Abe, J. *J. Am. Chem. Soc.* **2009**, *131*, 7256–7263.

(2) (a) Ohkoshi, S.-I.; Tsunobuchi, Y.; Matsuda, T.; Hashimoto, K.; Namai, A.; Hakoe, K.; Tokoro, H. *Nat. Chem.* **2010**, *2*, 539–545. (b) Crespo-Monteiro, N.; Destouches, N.; Bois, L.; Chassagneux, F.; Reynaud, S.; Fournel, T. *Adv. Mater.* **2010**, *22*, 3166–3170. (c) Zheng, L.; Xu, Y.; Jin, D.; Xie, Y. *Chem. Mater.* **2009**, *21*, 5681–5690. (d) Naoi, K.; Ohko, Y.; Tatsuma, T. *J. Am. Chem. Soc.* **2004**, *126*, 3664–3668. (e) He, T.; Yao, J. *J. Mater. Chem.* **2007**, *17*, 4547–4557. (f) Zhang, Y.; Lee, S.-H.; Mascarenhas, A.; Deb, S. K. *Appl. Phys. Lett.* **2008**, 92, 203508.

(3) (a) Russew, M.-M.; Hecht, S. *Adv. Mater.* **2010**, *22*, 3348–3360. (b) Wang, M.-S.; Xu, G.; Zhang, Z.-J.; Guo, G.-C. *Chem. Commun.* **2010**, *46*, 361–376. (c) Zhang, C.; Zhou, H.-P.; Lia, L.-Y.; Feng, W.; Sun, W.; Li, Z.-X.; Xu, C.-H.; Fang, C.-J.; Sun, L.-D.; Zhang, Y.-W.; Yan, C.-H. *Adv. Mater.* **2010**, *22*, 633–637. Qin, B.; Chen, H.; Liang, H.; Fu, L.; Liu, X.; Qiu, X.; Liu, S.; Song, R.; Tang, Z. *J. Am. Chem. Soc.* **2010**, *132*, 2886–2888.

(4) (a) Dolbecq, A.; Dumas, E.; Mayer, C. R.; Mialane, P. *Chem. Rev.* **2010**, *110*, 6009–6048. (b) Kortz, U.; Müller, A.; Salgeren, J. V.; Schnack, J.; Dalal, N. S.; Dressel, M. *Coord. Chem. Rev.* **2009**, *253*, 2315–2327. (c) Zhang, J.; Song, Y.-F.; Cronin, L.; Liu, T. *Chem.—Eur. J.* **2010**, *16*, 11320–11324. (d) Clemente-Leon, M.; Ito, T.; Yashiro, H.; Yamase, T. *Chem. Mater.* **2007**, *19*, 2589–2594. (e) Michaillovski, A.; Hussain, F.; Spingler, B.; Wagler, J.; Patzke, G. R. *Cryst. Growth Des.* **2009**, *9*, 755–765.

(5) (a) Long, D.-L.; Burkholder, E.; Cronin, L. *Chem. Soc. Rev.* **2007**, *36*, 105–121. (b) Dessapt, R.; Kervern, D.; Bujoli-Doeuff, M.; Deniard, P.; Evain, M.; Jobic, S. *Inorg. Chem.* **2010**, *49*, 11309–11316. (c) Hubbard, D. J.; Johnston, A. R.; Sanchez Casalongue, H.; Narducci Sarjeant, A.; Norquist, A. J. *Inorg. Chem.* **2008**, *47*, 8518–8525. (d) Tan, H.; Li, Y.; Chen, W.; Liu, D.; Su, Z.; Lu, Y.; Wang, E. *Chem.—Eur. J.* **2009**, *15* 10940–10947.

(6) (a) Yamase, T. *Chem. Rev.* **1998**, *98*, 307–325. (b) He, T.; Yao, J. *Prog. Mater Sci.* **2006**, *51*, 810–879. (c) Coué, V.; Dessapt, R.; Bujoli-Doeuff, M.; Evain, M.; Jobic, S. *Inorg. Chem.* **2007**, *46*, 2824–2835. (d) Compain, J.-D.; Deniard, P.; Dessapt, R.; Dolbecq, A.; Oms, O.; Sécheresse, F.; Marrot, J.; Mialane, P. *Chem. Commun.* **2010**, *46*, 7733–7735. (e) Liu, S.; Möhwald, H.; Volkmer, D.; Kurth, D. G. *Langmuir* **2006**, *22*, 1949–1951.

(7) Dessapt, R.; Collet, M.; Coué, V.; Bujoli-Doeuff, M.; Jobic, S. *Inorg. Chem.* **2009**, *48*, 574–580.

(8) H_2DABCO^{2+} ($N_2C_6H_{14}{}^{2+}$) and $HDMA^+$ ($(CH_3)_2NH_2{}^+$) correspond to the diprotonated 1,4-diazabicyclo[2.2.2]octane and the dimethylammonium cations, respectively.

(9) Jobic, S.; Coué, V.; Bujoli-Doeuff, M.; Dessapt, R. Patent WO2009030831, 2009.

(10) Weiner, H.; Lunk, H. J.; Stoesser, R.; Lueck, R. *Z. Anorg. Allg. Chem.* **1989**, *572*, 164–174.

(11) Burla, M. C.; Caliandro, R.; Camalli, M.; Carrozzini, B.; Cascarano, G. L.; De Caro, L.; Giacovazzo, C.; Polidori, G.; Spagna, R. *J. Appl. Crystallogr.* **2005**, *38*, 381–388.

(12) Petricek,V.; Dusek, M.; Palatinus, L. *JANA 2006, a Crystallographic Computing System, Institute of Physics*; Academy of Sciences of the Czech Republic: Prague, Czech Republic, 2000.

(13) Brandenburg, K. *Diamond*, version 3; Crystal Impact GbR: Bonn, Germany, 2001.

(14) Kubelka, P.; Munk, F. *Z. Techn. Physik* **1931**, *12*, 593–601.